J Mater Sci (2024) 59:16862–16883

Ceramics

Quantitative analysis of grain boundary segregation and fracture behavior in Ca-doped magnesium aluminate spinel

Alexander Campos-Quiros[1,*], Metri Zughbi[1], Animesh Kundu[2], and Masashi Watanabe[1,3]

[1] *Department of Materials Science and Engineering, Lehigh University, 5 East Packer Avenue, Bethlehem, PA 18015, USA*
[2] *Department of Mechanical Engineering and Mechanics, Lehigh University, 19 Memorial Drive West, Bethlehem, PA 18015, USA*
[3] *Institute for Materials Research, Tohoku University, 2-1-1 Katahira, Aoba-ku, Sendai, Miyagi 980-8577, Japan*

Received: 11 June 2024
Accepted: 28 August 2024
Published online: 13 September 2024

ABSTRACT

Grain boundary structure and chemistry play crucial roles in determining atomic diffusion, grain growth, and mechanical behavior in magnesium aluminate spinel ($MgAl_2O_4$, spinel). The grain boundary structure and chemistry can be modified by doping with cations, such as Ca^{2+}, to facilitate grain boundary segregation and tailor such properties. However, the nanoscale details of the segregation behavior of calcium and its mechanism, and hence the dopant behavior influence on the grain boundary mechanical properties, have not yet been clearly understood. In this study, the segregation behavior of Ca^{2+} in spinel was quantitatively analyzed by X-ray energy dispersive spectrometry (XEDS) and electron energy-loss spectrometry (EELS), and compared to undoped spinel. Composition profiles obtained from EELS spectrum-imaging datasets across grain boundaries showed calcium segregation at the boundary core correlated with magnesium depletion. Additionally, energy-loss near-edge structure (ELNES) analysis of the Mg–K edge indicated that changes in the bonding status of the Mg^{2+} sublattice occurred after Ca-doping. It is implied that Ca^{2+} cations replace Mg^{2+} at tetrahedral sites in spinel. The calcium enrichment at grain boundaries obtained through quantitative XEDS analysis was in the range of 0.1–0.9 atoms/nm^2 (0.03—0.26 monolayers). Calcium segregation had no detrimental effect on the indentation fracture toughness estimated through microindentation. The fracture behavior remains unaltered compared to undoped spinel, presenting primarily transgranular cracking. These results suggest that magnesium replacement by calcium atoms at the grain boundary core occurred with no compromise on the fracture toughness or fracture behavior, allowing it to maintain similar mechanical integrity as undoped spinel.

Handling Editor: David Cann.

Address correspondence to E-mail: ajc420@lehigh.edu

https://doi.org/10.1007/s10853-024-10171-z

GRAPHICAL ABSTRACT

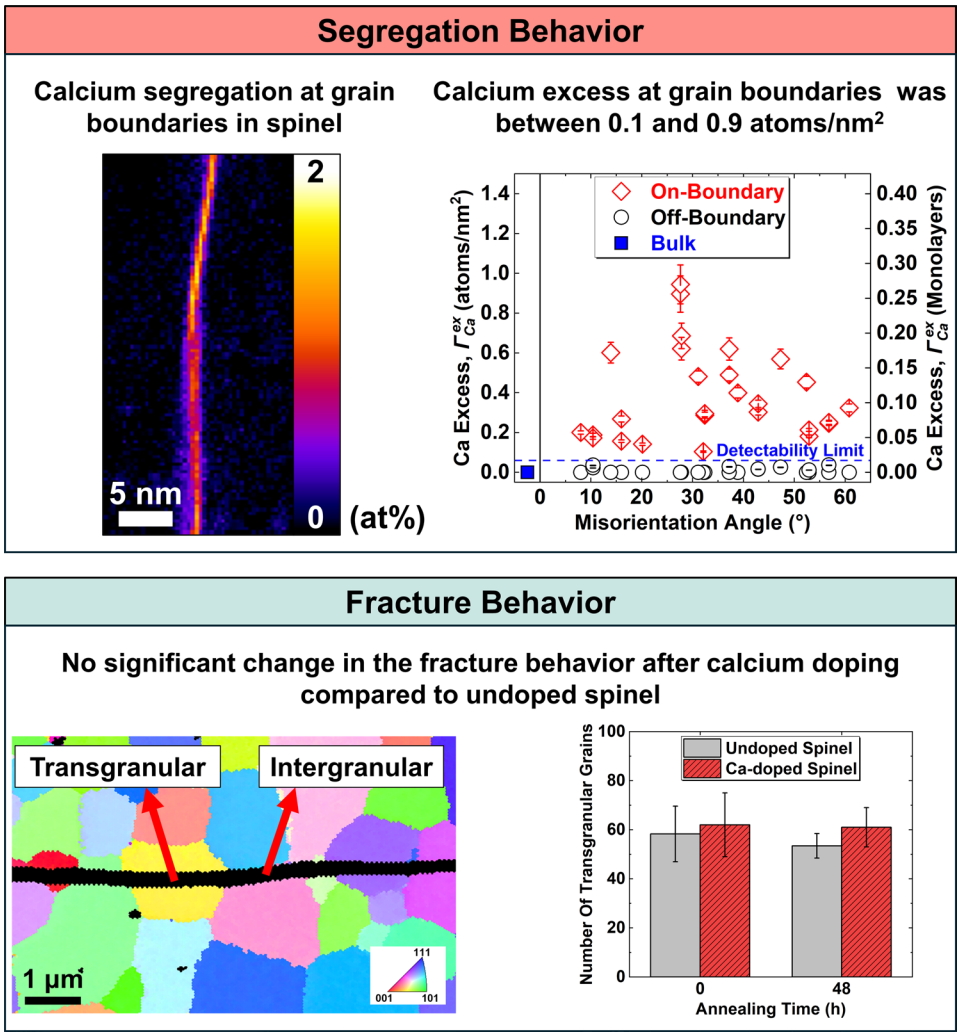

Introduction

Polycrystalline magnesium aluminate spinel with near theoretical density, or simply spinel ($MgAl_2O_4$), is a transparent ceramic material of great interest for application in extreme environments where low density and excellent chemical, thermal, and radiation resistance are required. In contrast with other conventional transparent ceramic materials, such as fused silica [1], spinel combines outstanding high transparency from ultraviolet to mid-infrared wavelengths (~ 190 nm to ~ 6000 nm) with remarkable mechanical properties such as high hardness (16.5 GPa), elastic modulus (260 GPa), and flexural strength (250 MPa) [2]. These properties make spinel attractive for fabricating transparent windows and domes for aircraft, submarines, and transparent armor operating in extremely harsh environments [3]. It should be noted that, for those applications, high fracture toughness is one of the critical requirements.

The grain boundary structure and chemistry play significant roles in determining the fracture toughness in polycrystalline spinel, as the segregation of dopant atoms can affect the mechanical properties of the grain boundaries. In stoichiometric normal $MgAl_2O_4$, Mg^{2+} is present in tetrahedral sites with an ionic radius of 57 pm and Al^{3+} in octahedral sites with an ionic radius of 54 pm [4], but cationic site disordering and inversion can occur due to doping,

higher temperature or irradiation. One important aspect to facilitate grain boundary segregation instead of substitutional incorporation in the lattice is selecting dopants with ionic radii (r_i) larger than host cations. For this reason, rare-earth cations, such as ytterbium (Yb^{3+}, $r_i = 87$ pm) and europium (Eu^{2+}, $r_i = 117$ pm), have been previously studied as dopants [4–6]. For example, Cao et al. reported increased fracture toughness in Yb-doped spinel [5]. The fracture toughness was measured by in-situ microcantilever testing of individual grain boundaries. The enhanced fracture toughness was attributed to the segregation of ytterbium in the grain boundaries. The presence of ytterbium in the grain boundaries was confirmed by direct observation of the identical grain boundaries by atomic-resolution scanning transmission electron microscopy (STEM) imaging. It was found that Yb presented a tendency to form a monolayer of staggered pairs at the grain boundary. Also, it was hypothesized that the enhanced grain boundary cohesion after doping could be linked to the formation of stronger Yb-O bonds at the interface. In another study by Cui et al., the fracture toughness of individual grain boundaries measured by microcantilever testing remained unaltered after Eu doping compared to undoped spinel [6]. These results suggest that a deeper understanding of the grain boundary segregation behaviors of dopant elements in spinel is necessary to predict the grain boundary mechanical properties. Additionally, more abundant and inexpensive dopants are preferable to rare-earth elements for mass-production purposes to utilize spinel materials in extreme environments.

One promising candidate to substitute rare-earth doping in spinel is calcium. Previous studies have reported calcium segregation at grain boundaries in spinel [7, 8], enhanced densification [9–11], improved the modulus of rupture at elevated temperatures [12], and increased bulk fracture toughness [13]. However, most of these studies focused only on the bulk microstructure and mechanical properties, leaving aside more detailed characterizations at the nanoscale, such as the segregation level, the position of the dopant atoms at grain boundaries, and the relation between segregation and grain boundary mechanical properties. Consequently, the mechanism for enhanced mechanical properties has not yet been fully understood.

For example, in a study conducted by Kim et al. [8], calcium segregation at grain boundaries as well as Mg deficiency was confirmed by X-ray energy dispersive spectrometry (XEDS) analysis, but the Ca-doping level was not controlled, and a detailed quantitative analysis of the segregation behavior was not performed. In another study, Chiang et al. [7] determined that the Al/Mg and O/Mg intensity ratios increased at grain boundary positions by XEDS analysis, suggesting a complex space-charge layer in the vicinity of grain boundaries in spinel. The calcium segregation behaviors at grain boundaries and their influence on mechanical properties remain unknown.

In this study, the calcium segregation behavior at grain boundaries in spinel was quantitatively investigated by detailed XEDS and electron energy-loss spectrometry (EELS) analysis. The crack propagation behaviors induced by microindentation were also examined quantitatively through results obtained by electron backscattering diffraction (EBSD) analysis as an alternative to conventional qualitative fractography analysis. The quantification of the EBSD results provided detailed insights into the fraction of transgranular cracking and the frequency of intergranular fracture events as a function of the grain boundary misorientation angle. The primary focus of this study was on the grain boundary segregation behavior and its effect on microhardness, fracture toughness, and fracture behavior. The microstructure evolution as a function of time, temperature, and dopant concentration was not a focus for this work.

Experimental

Sample fabrication

High-purity spinel powder (Baikowski, S25CR) and $Ca(NO_3)_2{\cdot}4H_2O$ (99.98%, Alfa Aesar) were used to fabricate undoped and Ca-doped (500 ppm) spinel samples. The baseline line impurity concentration in the spinel powder utilized in this study was determined by glow discharge mass spectrometry. A calcium concentration of 5.1 ppm by weight was observed, which is not significant compared to the doped Ca level. The Mg/Al ratio was nominally 1.0 in the as-received powder. For the Ca-doped spinel sample, the $Ca(NO_3)_2{\cdot}4H_2O$ was dissolved in high-purity ethanol. A specific amount of the calcium nitrate solution was added to a weighted batch of spinel powder to produce a suspension with a nominal doping concentration of 500 ppm of calcium by

mole. The suspension was then thoroughly mixed using a magnetic stirrer to ensure homogeneity. Then, the suspension was dried under a vacuum to remove the excess ethanol.

Both the undoped spinel and the Ca-doped spinel powders were hot-pressed to near the theoretical density. A Thermal Technology LLC hot-press system (HP20-4560-20SS) was employed to fabricate the undoped and Ca-doped spinel samples. The hot-pressing was performed under vacuum. At the start of the experiment the vacuum was < 30 mTorr. A preload of 223 kg was applied to the sample at the start of the run. The hot-pressing cycle consisted of simultaneously increasing the temperature and load at a rate of 10 °C/min and 15 kg/min, respectively, until maximum values of 1250 °C and 2068 kg (40 MPa) were reached. The dwell time at the maximum temperature and load was 1 h. Then, all the load was removed in 1 min and the sample was cooled at 10 °C/min to room temperature.

The dimensions of the hot-pressed samples were nominally 25.4 mm in diameter and 10 mm in height. To avoid contamination from the graphite dies used during the hot-pressing step, only the core part of the sample was utilized in this study. The center core of the samples was extracted after removing ~ 1 mm each from the top and bottom surfaces of the cylinder. Then, a ~ 9 × 9 mm sample core was extracted by cutting off the sides of the cylindrical sample. The core part of the hot-press samples was sectioned into multiple smaller parts. One part of both undoped spinel and Ca-doped spinel samples was left in the as-hot-pressed condition and utilized for further microstructure and mechanical properties characterization. The remaining parts of the samples were annealed at 1400 °C for 24 and 48 h in an air atmosphere using a high-purity alumina tube, with heating and cooling rates of 5 °C/min to relieve residual stresses from the hot-pressing as well as allowing the dopants to diffuse and reach a thermodynamically stable state. The calcium doping level and subsequent heat treatments were selected based on previous studies in spinel doped with rare-earth elements where doping levels of 500 ppm were observed to be sufficient for affecting the microstructure and fracture behavior [14, 15]. Additionally, it is crucial to avoid secondary phase formation in studying the effect of calcium doping on the segregation behavior and mechanical properties. The segregation behavior of calcium atoms to the grain boundaries and its effect on the mechanical properties were studied in detail.

Bulk microstructure

For bulk electron microscopy observation, samples were mechanically polished, followed by finishing with a 50-nm diamond suspension. The bulk microstructure before and after annealing was investigated utilizing scanning electron microscopy (SEM) coupled with EBSD analysis in a dual beam focused ion beam (FIB) instrument (Thermo/Fisher Scientific Scios). SEM images were acquired at an acceleration voltage of 7 kV with a probe current of 0.8 nA using an in-lens backscattered electron detector. EBSD analysis was performed at an acceleration voltage of 12 kV and a probe current of 13 nA with a step size of 50 nm utilizing an EDAX Hikari camera. EBSD data analysis was performed using EDAX OIM software. The analysis procedure involved applying a neighbor pattern averaging & reindexing (NPAR) followed by a grain dilation with a minimum grain size of 8 pixels. For the grain size analysis, incomplete grains from the edges of the EBSD maps were ignored.

Segregation behavior

Electron transparent thin specimens were prepared using a Ga^+ beam in a FIB instrument (Thermo/Fisher Scientific Scios) operated at 30 kV. Damaged layers on the surface of FIB-prepared thin specimens were gently removed by a Fischione 1040 nanomill instrument at 900 eV. To determine the misorientation angles between grains in the thin lamella, transmission Kikuchi diffraction (TKD) analysis was performed using an acceleration voltage of 30 kV, a current of 26 nA, and a step size of 50 nm. To evaluate the dopant segregation behavior, detailed atomic-scale characterization was performed using high-angle annular dark-field (HAADF)-STEM imaging in an aberration-corrected STEM JEOL JEM-ARM200CF instrument operated at 200 kV. XEDS analysis using the ζ-factor method was carried out by a JEOL XEDS detector with a 100-mm^2 active area in the ARM200CF to quantify the calcium enrichment as a function of the grain boundary misorientation angle extracted from the TKD analysis [16]. 18 different grain boundaries (a total of 27 measurements on-boundary and 27 measurements off-boundary), as well as 3 grain interiors (a total of 5 measurements), were analyzed using the raster-scan box method. This method consisted of scanning the electron beam over an area of ~ 12 × 75

nm^2 while acquiring an XEDS spectrum with a collection time of 120 s. The center of the raster-scan box was aligned with the grain boundary for the on-boundary measurements, ~ 28 nm away from the grain boundary for the off-boundary condition, and several hundreds of nanometers away for the bulk measurements. Magnesium, aluminum, and oxygen concentrations were also determined for all measurements. The grain boundary excess of Ca (Γ_A^{ex}) was determined from the XEDS analysis following the equation [17]:

$$\Gamma_A^{ex} = N_B \frac{X_A^{gb} - X_A^{bk}}{X_B} \frac{V}{A} \tag{1}$$

Here, N_B is the number of B atoms per unit volume in the bulk region, X_A^{gb} and X_A^{bk} are the atomic fraction of dopant element A at the grain boundary and in the bulk region, X_B is the atomic fraction of element B in the bulk and V and A are the interaction volume and the grain boundary area inside the interaction volume. The selection of element B in Eq. (1) is of key importance in complex oxides such as spinel where two cation sublattices (Mg^{2+} tetrahedral and Al^{3+} octahedral sublattices) are present. For this reason, special attention was paid to elucidating the position of calcium atoms at the grain boundaries.

To gain information about the elemental distribution of the different elements in the grain boundary vicinity EELS analysis was performed by acquiring spectrum-imaging (SI) datasets through a CEOS energy filtering and imaging device (CEFID) equipped with a hybrid-pixel electron detector Dectris ELA. SI datasets were collected with an energy dispersion of 1.77 eV/channel over a range of 1820 eV. A convergence semi-angle (α) of 34 mrad and a collection semi-angle (β) of 60 mrad were used with a camera length of 2.5 cm. Furthermore, the SI datasets were acquired using CEOS Panta Rhei software, followed by principal component analysis (PCA) [18] in Gatan Digital Micrograph software to remove random noise. Subsequently, quantitative analysis was performed using the reconstructed SI dataset using the following equation [19]:

$$\frac{N_A}{N_B} = \frac{I_{KA}(\beta, \Delta)\sigma_{JB}(\beta, \Delta)}{I_{JB}(\beta, \Delta)\sigma_{KA}(\beta, \Delta)} \tag{2}$$

Here, N_A and N_B are the areal densities of elements A and B, $I_{KA}(\beta, \Delta)$ and $I_{JB}(\beta, \Delta)$ are the integrated intensities of the characteristic edges corresponding to elements A and B, $\sigma_{KA}(\beta, \Delta)$ and $\sigma_{JB}(\beta, \Delta)$ are the partial ionization cross-sections for elements A and B. The collection semi-angle β and integration window Δ (34.2 eV) were kept constant, and the subindices K and J denote that different edge families were used depending on the elements A and B energy-losses. Ca-$L_{2,3}$, O-K, Mg–K, and Al-K edges were used for the quantitative analysis using the Hartree-Slater ionization cross-section model. The errors in the EELS quantitative analysis were estimated considering statistical error following the equation [19]:

$$\Delta C_A = C_A \frac{3\sqrt{I_{KA} + hI_{bA}}}{I_{KA}} \tag{3}$$

$$h = \frac{I_{bA} + 3\sqrt{I_{bA}}}{I_{bA}} \tag{4}$$

Here, ΔC_A is the error associated with the relative composition of element A, C_A is the relative composition in atomic percent, I_{KA} is the integrated intensity of the edge after background subtraction over the range Δ corresponding to the element A, I_{bA} is the integrated intensity of the background below the integration region of the edge, and h is a dimensionless parameter associated with the uncertainty of the background extrapolation.

The high dynamic range of the Dectris ELA detector allowed for the acquisition of the highly intense zero-loss peak (ZLP) simultaneously with the low-intensity edges signals in a single spectrum without saturation. This enabled the calculation of the relative thickness of the specimen using the log-ratio method [19]:

$$t/\lambda = \ln\left(\frac{I}{I_0}\right) \tag{5}$$

Here, t is the specimen thickness, λ is the plasmon mean free path at 200 kV in spinel, I is the total intensity of the spectrum, and I_0 is the zero-loss peak intensity extracted from the SI dataset using a fitted logarithm tail model with a fit range of 4—6 eV. The t/λ relative specimen thickness term is expressed as a thickness with respect to the inelastic mean free path. All grain boundaries analyzed were performed at regions with relative thickness values below 1, which ensured that the effect of plural scattering was minimized. Hence, plural scattering deconvolution was not applied to the EELS-SI datasets.

Energy-loss near-edge structure (ELNES) analysis was performed in the vicinity of different grain boundaries in undoped and Ca-doped spinel to study the effect of calcium doping on the bonding state. For the ELNES analysis, the raster-scan box method was utilized which consisted of scanning the electron beam over an area of ~ 2 × 18 nm^2 while collecting a series of 30 EELS spectra with a dwell time of 1 s per spectrum. Then, the spectra were added together to enhance the signal-to-noise ratio and resolve subtle changes in the ELNES. An energy dispersion of 512 eV was used for the ELNES analysis (0.5 eV/pixel). The energy resolution measured as the full width at half maximum (FWHM) of the ZLP at the center of the ELA camera without a specimen was ~ 1.3 eV. Three series of spectra were recorded by shifting the spectrum position changing the liner drift tube (LT) voltage of the spectrometer to capture the ZLP (LT offset = 0 eV), Ca-$L_{2,3,}$ and O-K edges (LT offset = 515 eV) and Mg–K and Al-K edges (LT offset = 1500 eV). The ELNES analysis was performed on- and off-boundary. Subsequently, the different spectra were background subtracted using a power-law function, and the intensity was normalized by integrating the intensity in the continuum region (O: 607–657 eV, Mg: 1380–1430 eV and Al: 1635–1685 eV). Then, a qualitative analysis of the ELNES changes was performed to evaluate the effect of Ca doping.

Bulk mechanical properties

To determine both the effect of Ca-doping and annealing on the bulk mechanical properties, microindentation hardness measurements were performed following the ASTM-C1327-15 standard (an applied load of 1 kg, a dwell time of 10 s and a minimum of 30 indentations per sample) using a LECO LM 248AT microhardness tester [20]. The fracture toughness was determined using the Vickers indentation fracture (VIF) method using the following equation [21]:

$$K_c = 0.018\left(\frac{E}{H_v}\right)^{1/2}\left(\frac{P}{c^{3/2}}\right) \quad (6)$$

where K_c is the indentation fracture toughness, E is the elastic modulus (260 GPa [2]), H_v is the Vickers microhardness, P is the applied load during indentation, and c is the measured length of the cracks that emanate from the tips of the residual Vickers indentation marks. Only indentations with 4 straight primary cracks were used for the fracture toughness determination. Indentations with secondary cracks or spalled edges were disregarded in this analysis.

Crack propagation behavior

The crack propagation behavior analysis around the indentation area was conducted using SEM/EBSD analysis following the same acquisition conditions utilized for the bulk observations. NPAR followed by a grain dilation using EDAX OIM software was applied. A partition on the image quality was performed by removing the pixels from the crack regions without clear Kikuchi patterns. Subsequently, quantitative analysis was performed on the obtained EBSD maps from crack regions to determine the fraction of transgranular and intergranular cracking. For this, EBSD maps were converted to a grayscale and analyzed using Digital Micrograph software. A script was implemented that consisted of a 2-point comparison on both sides of the crack. Points with similar colors (or similar gray levels after conversion) on both sides of the crack were assigned as transgranular, whereas points with different colors were considered intergranular. This 2-point comparison was repeated along the whole length of the crack and the fraction of transgranular points was calculated.

To validate the results using the Digital Micrograph script, a similar process was performed using EDAX OIM software by manually selecting sets of points on both sides of the cracks. A minimum of about 200 grains per sample were analyzed. Cracks passing through grains with misorientation angles below 3 degrees were considered transgranular. Therefore, the fraction of transgranular cracking is simply the number of points with transgranular crack divided by the total number of points analyzed. Subsequently, a normalization to account for differences in crack length and grain size was performed using the equation:

$$n_{tg} = \text{transgranular length fraction}^* \frac{1}{d} \quad (7)$$

Here n_{tg} is the normalized number of transgranular grains along the crack path, l is the total crack length and d is the average grain size of the sample. Additionally, information regarding the grains that presented intergranular fracture was extracted by recording the misorientation angle on both sides of the crack and compared to the misorientation angle distribution from the bulk calculated using the method described

by Saylor et al. [22]. Finally, the distribution of coincident site lattice (CSL) grain boundaries with intergranular cracking was extracted from the crack regions.

Results

Bulk microstructure

Figure 1 shows the grain size distribution maps of as-hot-pressed undoped and Ca-doped spinel samples as well as annealed samples at 1400 °C for 48 h, obtained by EBSD analysis. Both undoped and Ca-doped spinel samples had similar grain size distributions in the as-hot-pressed conditions. After annealing, the overall grain size distributions were broadly similar for undoped and Ca-doped samples as well. The average grain size for Ca-doped spinel (700 nm) was slightly smaller than that for undoped spinel (870 nm). Additionally, a very small number of abnormally large grains were sporadically observed in a few locations in the Ca-doped spinel sample after annealing (see supplementary note 1). The total area of the large grains was estimated to be less than 5%. Although these abnormally large grains might have an influence on the segregation behavior of the more prominent population with a smaller grain size, their volume was insignificant to affect the mechanical properties (microhardness, indentation fracture toughness and crack propagation behavior) of interest for this study. Note that microindentation was performed in normal grain size regions to avoid any influence from abnormal grain growth. Therefore, they were not included in this study.

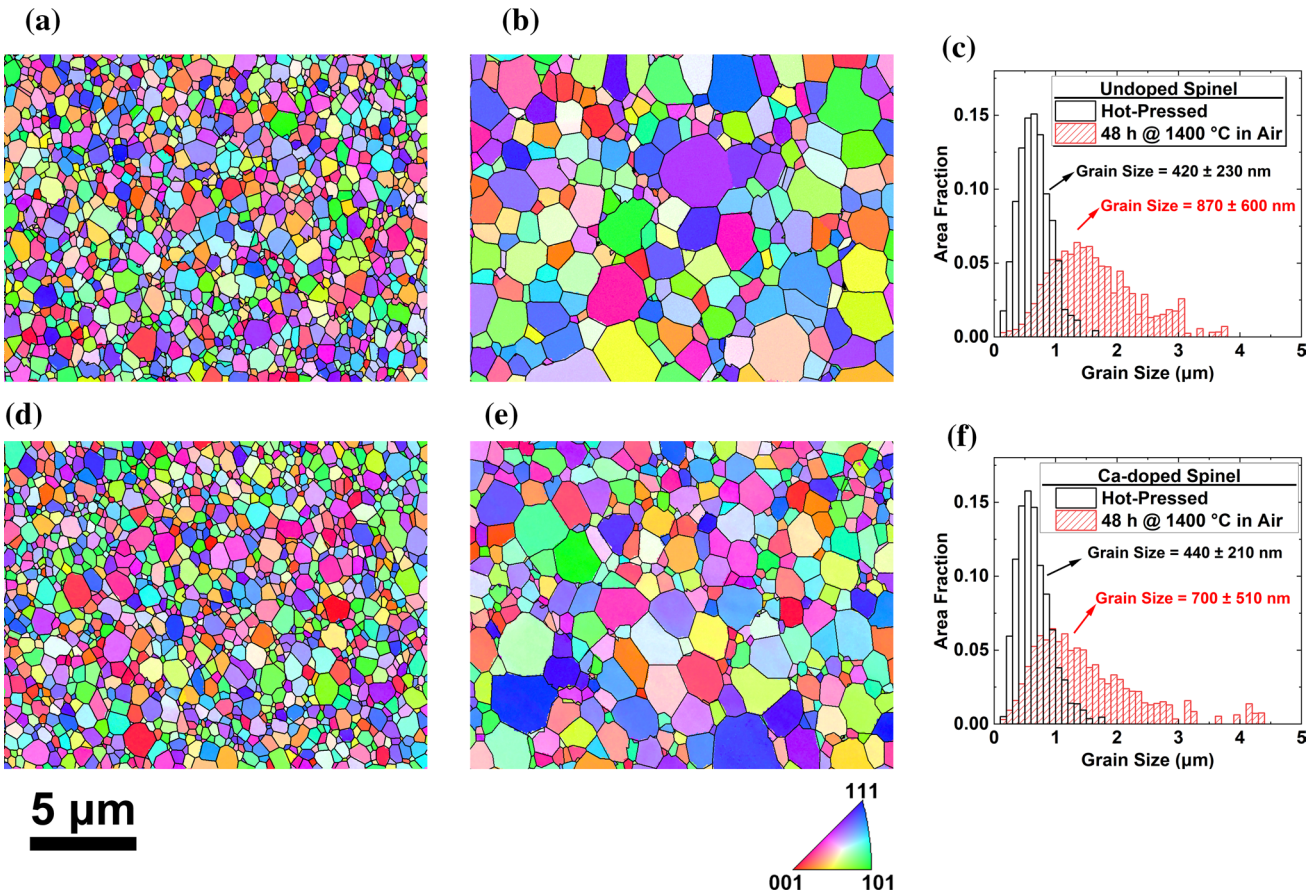

Figure 1 Results of EBSD analysis of undoped spinel **a** as-hot-pressed and **b** after annealing at 1400 °C for 48 h and Ca-doped spinel **d** as-hot-pressed and **e** after annealing at 1400 °C for 48 h. The grain size distributions for undoped and Ca-doped spinel samples are also shown in **c** and **f**, respectively. The dark solid lines in all the EBSD maps represent the reconstructed grain boundaries obtained from the OIM software.

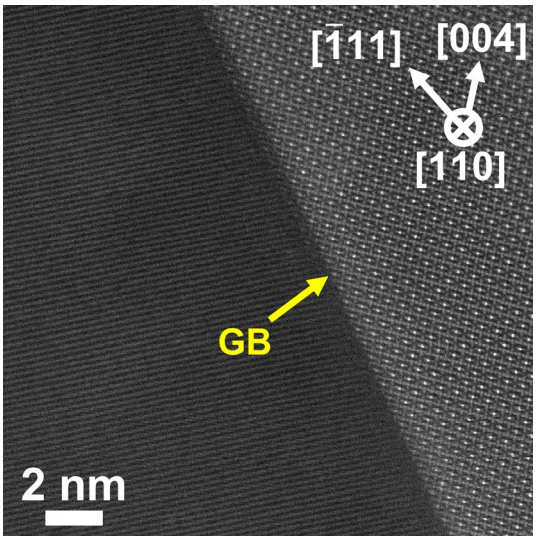

Figure 2 A representative HAADF-STEM image of a grain boundary in Ca-doped spinel after annealing for 48 h at 1400 °C showing the absence of secondary phases. Calcium segregation at grain boundaries was not visible due to low atomic number difference versus magnesium and aluminum.

Ca segregation behavior at grain boundaries

Figure 2 shows a representative HAADF-STEM image of a grain boundary in Ca-doped spinel close to an edge-on condition. Due to the relatively low atomic number difference between Ca ($Z = 20$) and host cations Mg ($Z = 12$) and Al ($Z = 13$), no enhanced intensity was found at the grain boundary indicative of calcium segregation. Additionally, no secondary phases were observed in any of the grain boundaries analyzed. For this reason, XEDS quantitative analysis was employed to confirm the segregation behavior of calcium atoms at grain boundaries.

The XEDS quantitative results were coupled with the misorientation angles between grains determined from the TKD maps of the FIB lamella (See supplementary note 2). Figure 3 shows the concentration of calcium, magnesium, aluminum, and oxygen as a function of the misorientation angle of the grain boundary analyzed on- and off-boundary as well as in the bulk. Calcium segregation was observed in all 18 grain boundaries analyzed in this study and limited

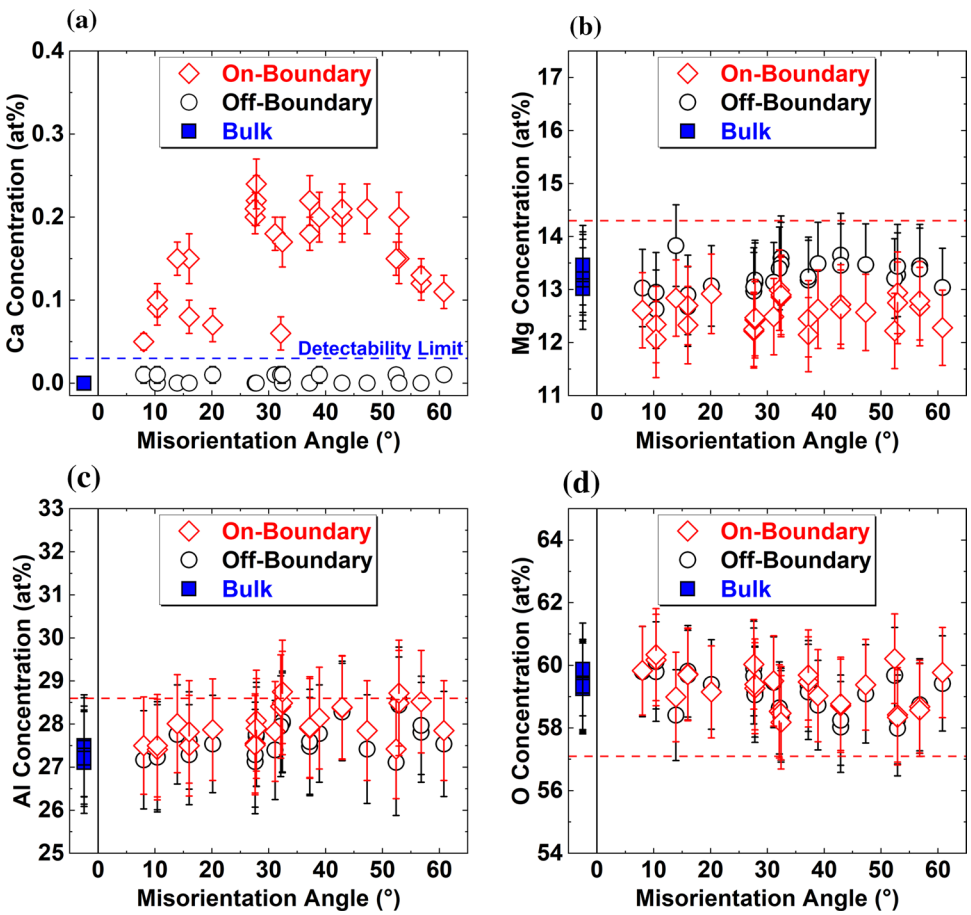

Figure 3 Concentration of **a** calcium, **b** magnesium, **c** aluminum, and **d** oxygen obtained from quantitative XEDS analysis using the ζ-factor method in the vicinity of different grain boundaries, plotted as a function of misorientation angle. The red horizontal dashed lines in (**a**-**d**) represent the stoichiometric composition of spinel (Mg: 14.3 at%, Al: 28.6 at%, and O: 57.1 at%) and the error bars represent a 99% confidence limit ($\pm 3\sigma$). The detectability limit for calcium was ~ 0.03 ± 0.02 at%, estimated from the fluctuation of background intensities under the Ca-Kα peakased on the criterium for a minimum detectable peak ($I > 3\sqrt{2B}$, where I is the peak intensity above the background B [24].

to the on-boundary position, as shown in Fig. 3a. Previous studies have shown that the amount of CaO in solid solution with spinel was negligible (below the detectability limit of 0.3 wt%) in samples quenched in air from a temperature as high as 1650 °C [23]. In this study, no calcium signal was detected in the bulk or off-boundary positions based on the minimum detection limit of the XEDS analysis employed in this study of ~ 0.03 ± 0.02 at% (~ 0.06 ± 0.03 wt%). Therefore, the amount of Ca in bulk regions in the spinel sample annealed at 1400 °C for 48 h and subsequently cooled at a rate of 5 °C/min is considered negligible as well. Additionally, the magnesium concentration was lower in the boundary compared to the off-boundary position (~ 28 nm away from the boundary) and the bulk (center of the grain). Conversely, the aluminum concentration was higher in the boundary compared to bulk measurements but did not show a significant difference with the off-boundary position. Also, the oxygen concentrations remained unaltered on and off the boundary compared to the bulk. (For detailed statistical analysis see supplementary note 3).

To better understand the spatial distribution of the different elements, EELS-SI datasets were collected in the vicinity of grain boundaries in undoped and Ca-doped spinel. Figure 4 shows the EELS quantitative analysis for undoped spinel. Figure 4a shows the HAADF-STEM image acquired simultaneously with the SI. The dark regions in the HAADF image indicate that some beam damage has occurred, but these regions did not affect the quantitative results as they are mainly located away from boundary position.

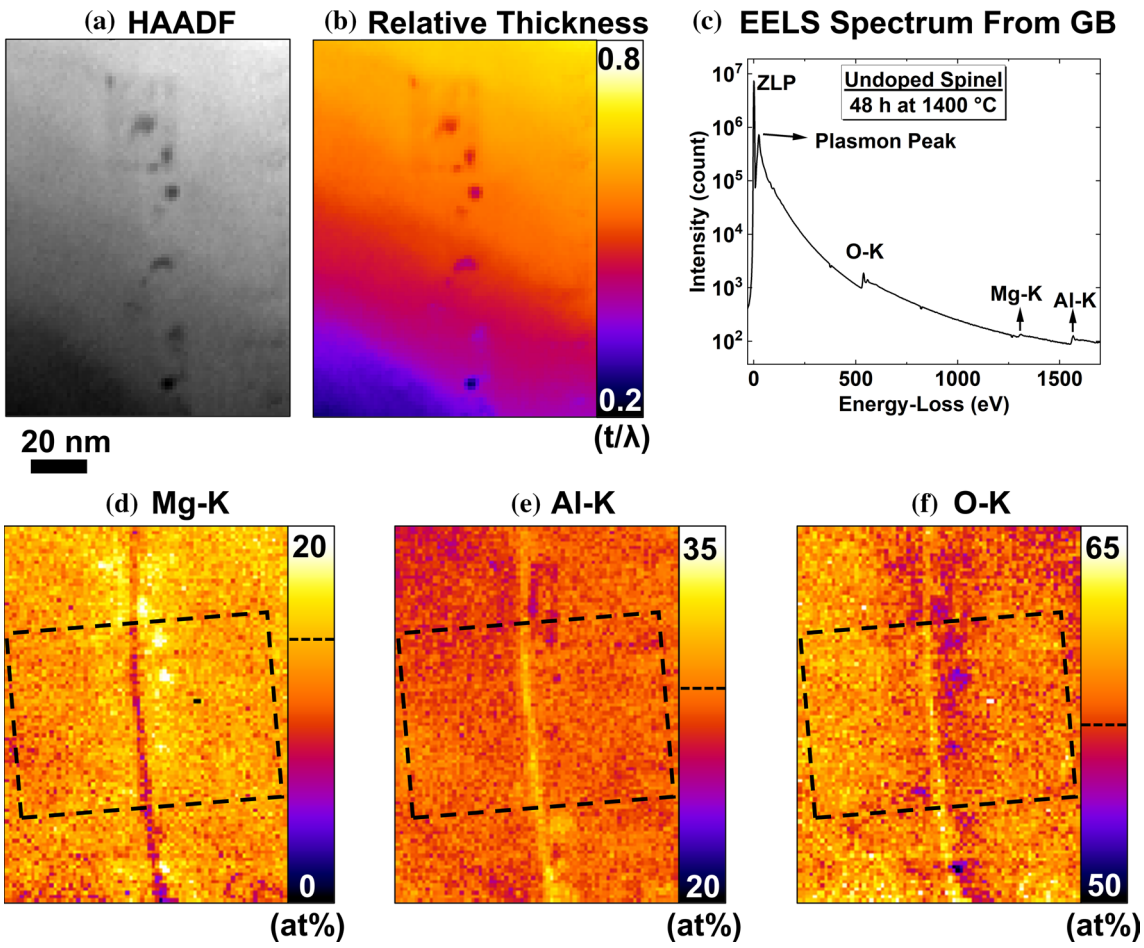

Figure 4 **a** A HAADF-STEM image acquired simultaneously with an EELS-SI in the vicinity of a grain boundary in the undoped spinel after annealing at 1400 °C for 48 h. **b** Relative specimen thickness and **c** a representative EELS spectrum used for the quantitative analysis of the concentration maps corresponding to **d** Mg–K, **e** Al -K, and **f** O-K ionization edges. The black dashed lines in the lookup table in (**d**-**f**) correspond to the composition of stoichiometric spinel (Mg: 14.3 at%, Al: 28.6 at%, and O: 57.1 at%).

Figure 4b shows the variation in relative thickness throughout the analyzed area. Since the obtained values of t/λ were below 1, no plural scattering deconvolution was applied prior to the quantitative analysis. Figure 4c shows a representative EELS spectrum in a semi-logarithmic plot where the high dynamic range of the detector enabled the acquisition of the high-intensity ZLP together with less intense Mg–K and Al-K edges. The undoped spinel specimen exhibited a clear magnesium deficiency at the grain boundary (Fig. 4d) as well as aluminum (Fig. 4e) and oxygen (Fig. 4f) excess. This change in composition (non-stoichiometry) in the grain boundary vicinity indicates the presence of a space-charge layer in undoped spinel, as reported in previous studies [7, 25–28].

Figure 5 shows the results obtained from an EELS-SI dataset taken from the vicinity of a grain boundary in Ca-doped spinel. Figure 5a shows a HAADF-STEM image acquired simultaneously with the EELS-SI dataset. The dark regions in the HAADF image indicate that some beam damage has occurred as well, but this damage is restricted only to the bottom right of the map and it is believed to have not affected the quantitative analysis, especially at the grain boundary position. Since the relative specimen thickness t/λ shown in Fig. 5b is below 1, no plural scattering

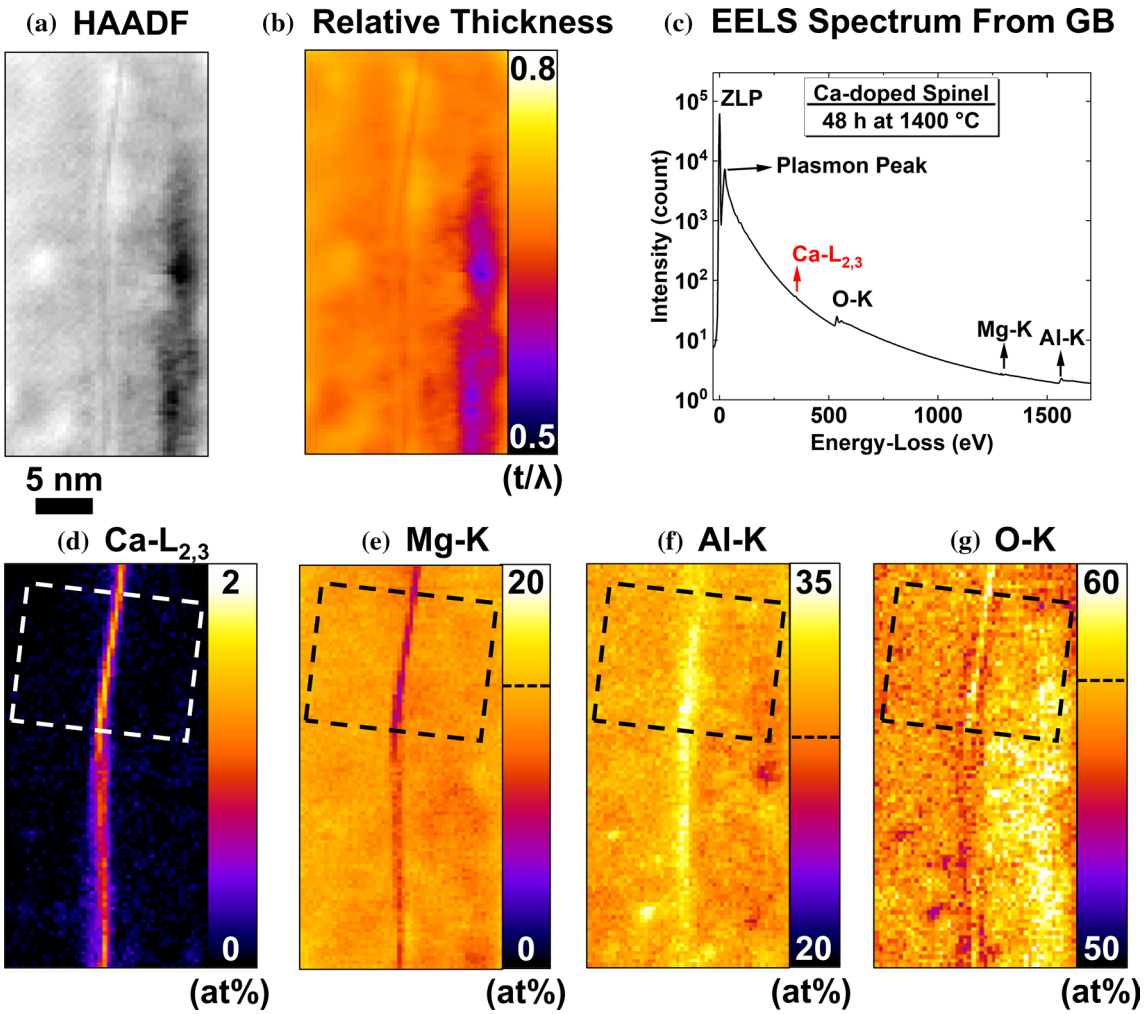

Figure 5 **a** A HAADF-STEM image acquired simultaneously with an EELS-SI in the vicinity of a grain boundary in Ca-doped spinel after annealing at 1400 °C for 48 h. **b** Relative specimen thickness and **c** a representative EELS spectrum used for the quantitative analysis of the concentration maps corresponding to **d** Ca-$L_{2,3}$, **e** Mg–K, **f** Al -K, and **g** O-K ionization edges. The black dashed lines in the lookup tables in (**e**–**g**) correspond to the composition of stoichiometric spinel (Mg: 14.3 at%, Al: 28.6 at%, and O: 57.1 at%).

deconvolution was applied prior to the quantitative analysis. Figure 5c shows a representative EELS spectrum from the grain boundary region where O-K, Ca-$L_{2,3}$, Mg–K, and Al-K edges are shown. From the composition maps obtained by the EELS quantification, clear calcium segregation (Fig. 5d), as well as magnesium depletion (Fig. 5e) along the grain boundary, were observed. The calcium and magnesium concentrations seem to be correlated since the top region of the grain boundary with higher calcium concentration shows a more considerable magnesium depletion compared to the bottom half. This inhomogeneity in the calcium concentration within the same grain boundary could be a consequence of the different facets on the top and bottom sections of the grain boundary, i.e., different grain boundary characters (GBCs). The distinct GBC between the top and bottom section is expected as the grain boundary changes its direction with respect to the adjacent grains forming the boundary. This would create different grain boundary planes and, therefore, different free volumes available for calcium atoms to segregate at the grain boundary.

The calcium excess and magnesium depletion are in good agreement with the quantitative analysis by XEDS in Fig. 3. This is in line with Fig. 3a where calcium segregation (at%) on the boundary is high at ~ 30–50 degree misorientation angle and low at other angles. However, aluminum and oxygen excess were also found in the grain boundary. The discrepancy could be related to the size of the analyzed area in the XEDS analysis compared to the EELS analysis. For the XEDS analysis, relatively large boxes (~ 12 × 75 nm^2) were set for on- and off-boundary conditions. Thus, the aluminum and oxygen concentrations were rather averaged out within the box and fine variations between the on- and off-boundary positions were not detected. In the case of the EELS-SI dataset, a complete spectrum is acquired at every pixel position with sub-nanometer step size. This allowed for the detection of more subtle composition variations at the grain boundary with a high spatial resolution that reduced the contribution from the matrix. Even for the XEDS analysis, a 1D line-profile acquisition may be essential instead of the box acquisition approach in order to observe subtle changes in the aluminum and oxygen compositions.

To better visualize the spatial distribution of the different elements in the grain boundary vicinity, concentration profiles from the regions indicated by boxes in Figs. 4 and 5 constructed by integrating the concentration maps perpendicular to the grain boundary are shown in Fig. 6. In the case of undoped spinel (Fig. 6a), a clear magnesium depletion is observed at the grain boundary accompanied by aluminum and oxygen excess. The concentration profiles for calcium and magnesium in Ca-doped spinel had similar shapes, as presented in Fig. 6b. Conversely, the concentration profile corresponding to aluminum appeared broader than that of calcium and magnesium. A spatial resolution of 2.2 ± 0.2 nm was calculated using the ζ-factor method assuming a Gaussian beam-broadening model and taking into account the determined thickness value for the same grain boundary shown in Fig. 6b. This spatial resolution can explain the width of calcium peak of around 2 nm (FWTM: full width at tenth maximum, which contains 90% of incident electrons). Therefore, calcium segregation can be still assumed to be restricted to the grain boundary core.

Qualitative ELNES analysis was conducted to determine if the addition of Ca affected the state of bonding of the different species at the grain boundary position. To directly compare the undoped spinel and the Ca-doped spinel specimens, the spatial difference method was used to sample areas with similar t/λ to minimize any effect from plural scattering. Figure 7 shows the ELNES analysis in the vicinity of a grain boundary in undoped spinel specimen (top) and Ca-doped spinel (bottom). The spectra were recorded on- and off-boundary, normalized in the continuum regions, and then the difference between the off- and on-boundary conditions was calculated. The relative thickness in the vicinity of the grain boundary position for undoped spinel was ~ 0.4 t/λ, while the relative thickness for Ca-doped spinel was ~ 0.6 t/λ. Therefore, no significant changes in the ELNES due to thickness effects are expected to occur. Figure 7a shows the ELNES for the Mg–K edge for undoped spinel where two principal peaks labeled as A and B and two pre-peaks labeled as A′ and A″ can be distinguished. The main difference between the on- and off-boundary conditions is the relative peak intensity, where the on-boundary ELNES presented lower intensity than the off-boundary conditions. Figure 7b shows the ELNES for the Al-K edge with 3 main peaks identified as A, B, and C. In this case, there are no significant changes in the ELNES between the on- and off-boundary analysis, as evidenced by a relatively flat difference plot. Figure 7c shows the ELNES corresponding to the O-K edge where 4 main peaks A, B, C, and D were identified,

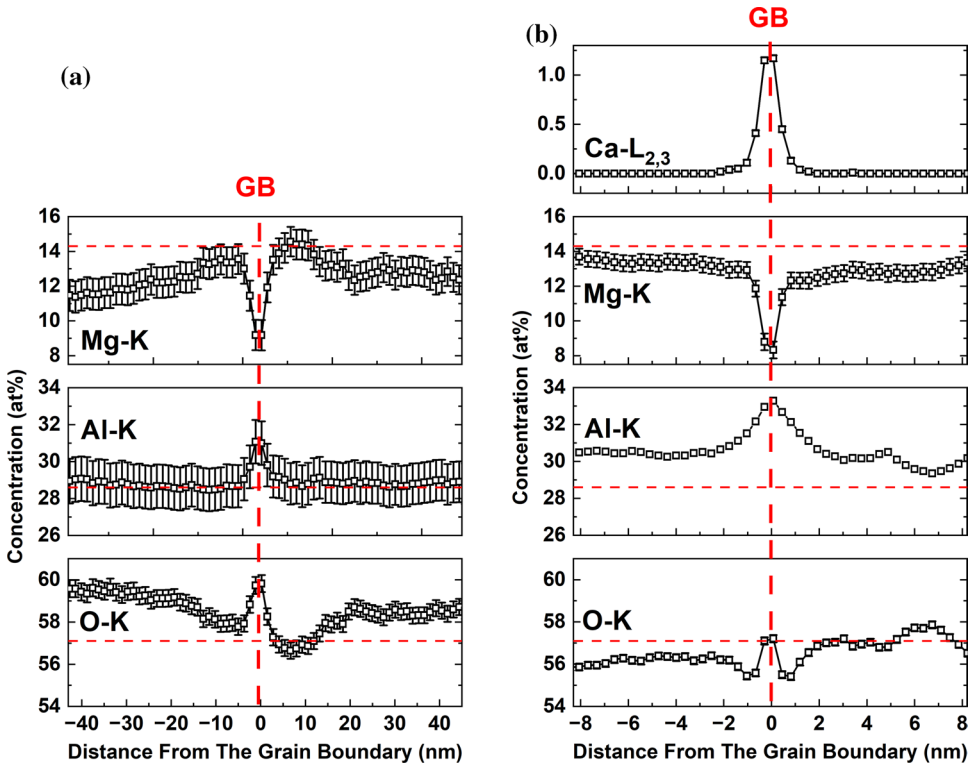

Figure 6 Concentration profiles extracted from the box regions indicated in Figs. 4 and 5 for **a** undoped spinel and **b** Ca-doped spinel. The error bars represent a 99% confidence limit (±3σ), and the horizontal dashed lines correspond to the stoichiometric composition of spinel (Mg: 14.3 at%, Al: 28.6 at%, and O: 57.1 at%).

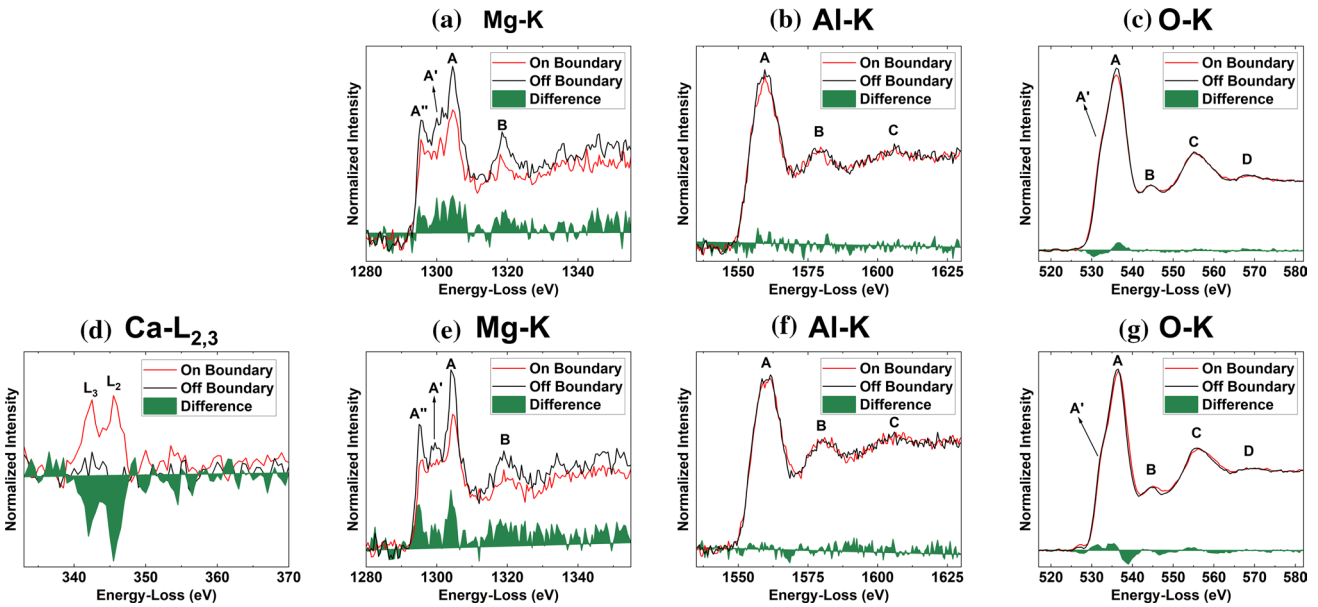

Figure 7 Comparison of ELNES in terms of **a** Mg–K, **b** Al-K, **c** O-K edges in undoped spinel as well as **d** Ca-$L_{2,3}$, **e** Mg–K, **f** Al-K and **g** O-K edges in Ca-doped spinel. A power-law background subtraction was applied to all edges, and the intensities were normalized from 1380–1430 eV for Mg, 1635–1685 for Al, and 607–657 eV for O, respectively.

as well as a pre-peak A′. The main difference between the on- and off-boundary conditions is the intensity of the A and A′ peaks: The A peak has a slightly higher intensity off-boundary, and the A′ has a slightly higher intensity on-boundary. The shape and number of peaks of the ELNES of these 3 elements are in good

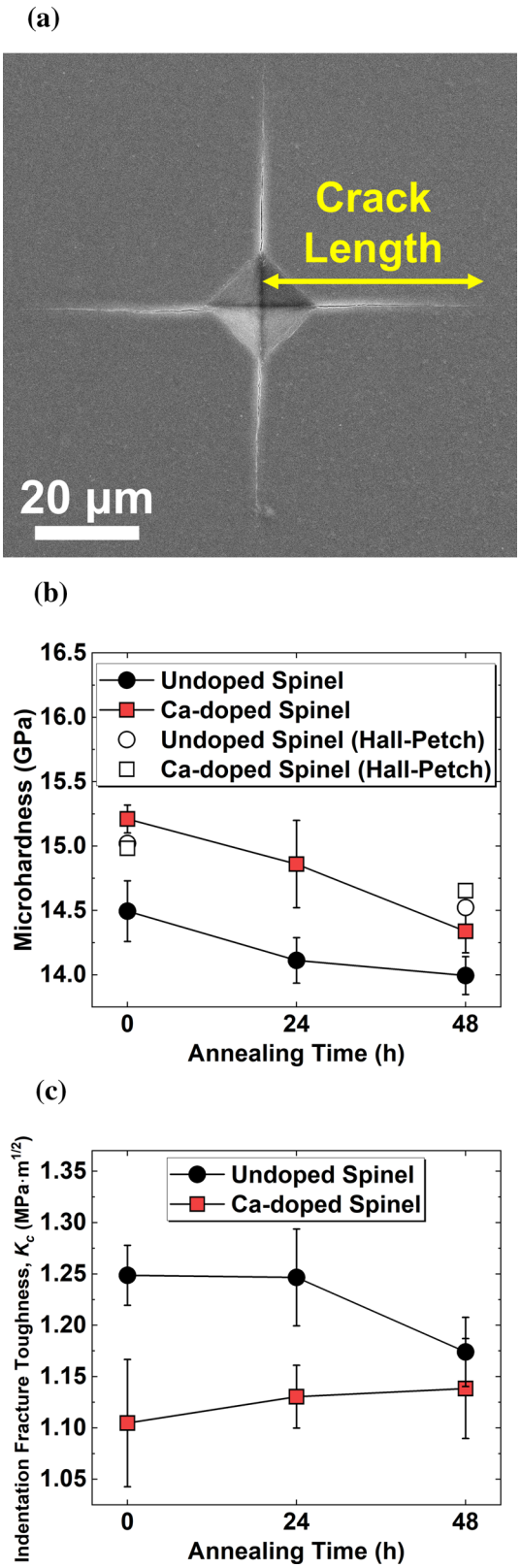

Figure 8 **a** Representative residual indentation mark produced by Vickers microhardness testing. **b** Vickers microhardness and **c** indentation fracture toughness of undoped and Ca-doped spinel as a function of annealing time at 1400 °C. Predicted microhardness values from the Hall–Petch relation in **b** were obtained using the expression reported elsewhere [31] for spinel.

agreement with previous results for undoped spinel [29].

In the case of Ca-doped spinel, Fig. 7d shows the Ca-$L_{2,3}$ signal on the boundary position. Moreover, no signal was found off the boundary, which indicated that Ca concentration in the matrix, if any, is below the detectability limit for the EELS analysis. Figure 7e shows the Mg–K ELNES for on- and off-boundary locations. The intensity of the on-boundary conditions is lower compared to off-boundary, similar to the undoped spinel condition. The main difference in the Mg–K ELNES between on- and off- boundary is the intensity of A′ pre-peak, which significantly decreases at the grain boundary position. This might indicate that Ca incorporation into the grain boundary could influence the bonding status of Mg atoms. However, a more quantitative analysis is required with theoretical estimation to assess if these changes could be linked to changes in the grain boundary cohesion. Figure 7f shows the ELNES for Al-K edge where the intensity did not change significantly between on- and off-boundary. Finally, Fig. 7g shows the ELNES for the O-K edge, where the main difference is found around the A and A′ peaks.

Bulk mechanical properties and fracture behavior

Figure 8a shows a representative indentation mark produced by Vickers microhardness testing. The microhardness of undoped and Ca-doped spinel samples calculated from the indentations are presented in Fig. 8b. The indentation fracture toughness calculated from the cracks extending from the indentation corners is presented in Fig. 8c. It should be mentioned that the actual values of fracture toughness from Vickers indentation are not reliable and cannot be used in place of single-edge-precracked-beam (SEPB) values (ASTM C1421), but these may be useful for relative comparison [30]. The decrease in microhardness in the annealed samples is simply due to the grain sizes, i.e., grain growth during annealing. Additionally, Ca-doped spinel had a higher microhardness compared

to undoped spinel. An analysis of the hardness following the Hall–Petch relation was performed. The results indicated that the expected hardness values based on the average grain size obtained by EBSD analysis are consistently closer to the measured values for Ca-doped spinel compared to the undoped spinel. In contrast, the fracture toughness is lower for Ca-doped spinel than that for the undoped spinel in the as-hot-pressed condition. However, the fracture toughness of Ca-doped spinel remains almost constant after annealing, while there is a decrease in the case of undoped spinel.

Figure 9 shows SEM images and corresponding EBSD maps along the cracks that emanate from the corners of the indentation marks after Vickers microhardness testing for undoped and Ca-doped spinel samples. The SEM images revealed that the undoped samples had higher porosity than the Ca-doped spinel (Fig. 4S). The lower microhardness observed in the undoped samples compared to Hall–Petch calculations and measurements for Ca-doped spinel could be a consequence of the higher porosity [32]. The cracks were relatively straight without noticeable branching. The EBSD maps showed regions along the crack where both transgranular and intergranular fractures were observed. It was difficult to distinguish the differences in fracture behavior from the EBSD maps obtained around the cracks. For this reason, a more thorough quantitative analysis of the crack propagation behavior was measured from the EBSD maps in terms of the relative transgranular fracture to the intergranular fracture.

Figure 10a shows a representative EBSD map in the vicinity of a crack in the undoped spinel sample with regions presenting transgranular and intergranular cracking propagations as indicated by arrows. Figure 10b shows the normalized number of transgranular grains along the crack path for both undoped and Ca-doped spinel samples before and after annealing. It was found that transgranular fracture was slightly less prevalent than intergranular fracture after annealing for each sample. Additionally, the samples after annealing showed a slightly higher number of transgranular fractured grains in Ca-doped spinel, which indicates that the grain boundary strength is preserved after calcium segregation to the grain boundaries as higher transgranular fracture indicates stronger grain boundaries than grain center (better grain-grain bonding).

Besides the transgranular fracture behavior, the grains that suffered intergranular fracture contain valuable information regarding the propensity of certain grain boundary types to fracture with a higher frequency. Figure 11a-b shows the misorientation angles of those grains from the crack regions that experienced intergranular fracture for undoped and Ca-doped

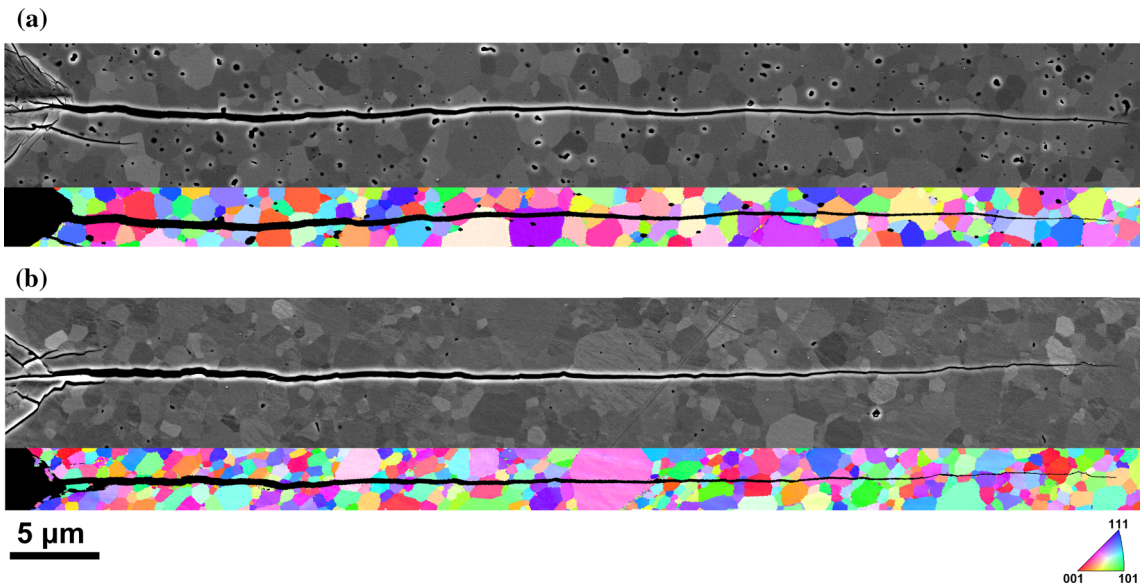

Figure 9 Two sets of a SEM image (top) and a corresponding EBSD map (bottom) of **a** undoped spinel and **b** Ca-doped spinel crack propagation behaviors after annealing at 1400 °C for 48 h.

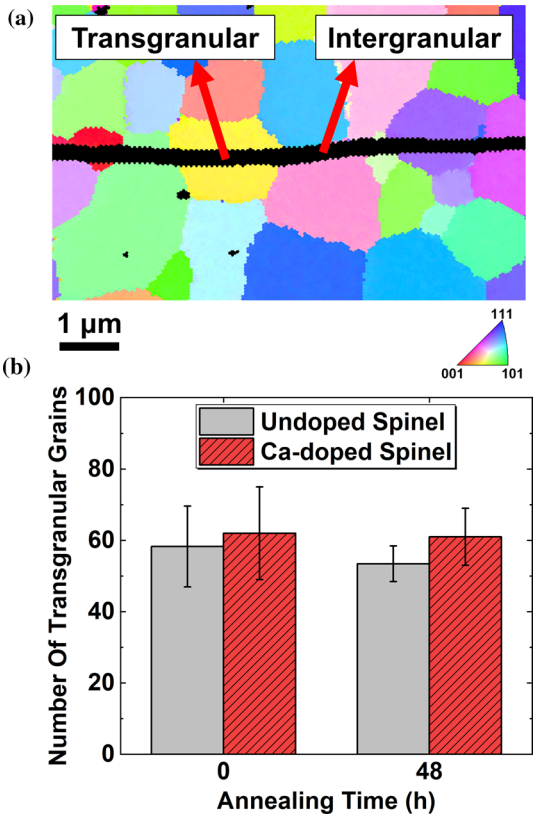

Figure 10 **a** Representative EBSD map consists of both transgranular and intergranular crack propagations, indicated by arrows. **b** Frequency of transgranular grains in the crack regions for undoped and Ca-doped spinel samples before and after annealing at 1400 °C for 48 h. The normalization factor for **b** considers the ratio of average crack length and grain size.

spinel samples after annealing, together with the misorientation angle distributions from the bulk. Both undoped and Ca-doped spinel samples presented a random distribution of grain boundary misorientations in the bulk and no preferential texture was evident. The misorientation angle of grain boundaries with intergranular cracking also follows a random distribution, and preferential cracking only occurred at low angles compared to the bulk. Figure 11c shows a more detailed characterization of the intergranular fracture as a function of the sigma value (Σ) of the coincidence site lattice (CSL) model. It is worth noting that CSL grain boundaries only account for ~ 8 percent of all the boundaries that suffered intergranular fracture, and the vast majority can be referred to as random grain boundaries. Low sigma grain boundaries such as Σ7 and Σ11 show less propensity to fracture in Ca-doped spinel, and this behavior is reversed for Σ23 and Σ29.

To summarize the intergranular fracture behavior analysis, Fig. 12 shows the normalized fraction of low(3-10)-, medium(10-45)- and high(45-63)-angle grain boundaries found along the crack path (intergranular cracking) for undoped and Ca-doped spinel samples compared to the bulk. A higher frequency of low- and medium-angle grain boundaries were found along the crack as compared to the bulk in the undoped and Ca-doped spinel samples (Figs. 12a, b). At high misorientation angles, the fraction of grains with intergranular cracking is slightly lower in the crack compared to the bulk in both undoped and Ca-doped spinel.

Discussion

Segregation behavior of calcium in spinel

The microstructures in the hot-pressed and annealed conditions for Ca-doped spinel samples were very similar to those in the undoped samples. The as-hot-pressed undoped spinel had higher porosity than Ca-doped spinel (~ 2.4% vs 0.2%), but after annealing the difference was reduced (~ 1.0% and 0.2%, respectively). The average grain size of the Ca-doped spinel sample was slightly smaller than that for undoped spinel (the difference was 700 nm vs 870 nm). The smaller grain size in the Ca-doped spinel sample indicates that calcium segregation to the grain boundaries might have limited the diffusion processes along (and across) the grain boundaries due to solute drag, ultimately affecting the grain growth. For confirmation, however, much longer annealing times at 1400 °C are required to observe additional grain growth and accentuate the effects of calcium segregation on the diffusion, presumably leading to a more discernable grain size difference. Additionally, a very small fraction of abnormally large grains (< 5%) was observed in the Ca-doped samples after annealing at 1400 °C for 48 h. A longer annealing time will also aid the development of the distinctive large grain size population in Ca-doped samples. The occurrence of abnormal grain growth might indicate the initiation of more prominent changes in the grain boundary plane and character distributions. Similar results have been found in Eu-doped spinel, where abnormal grain growth has been previously reported [15, 33]. Because of the small

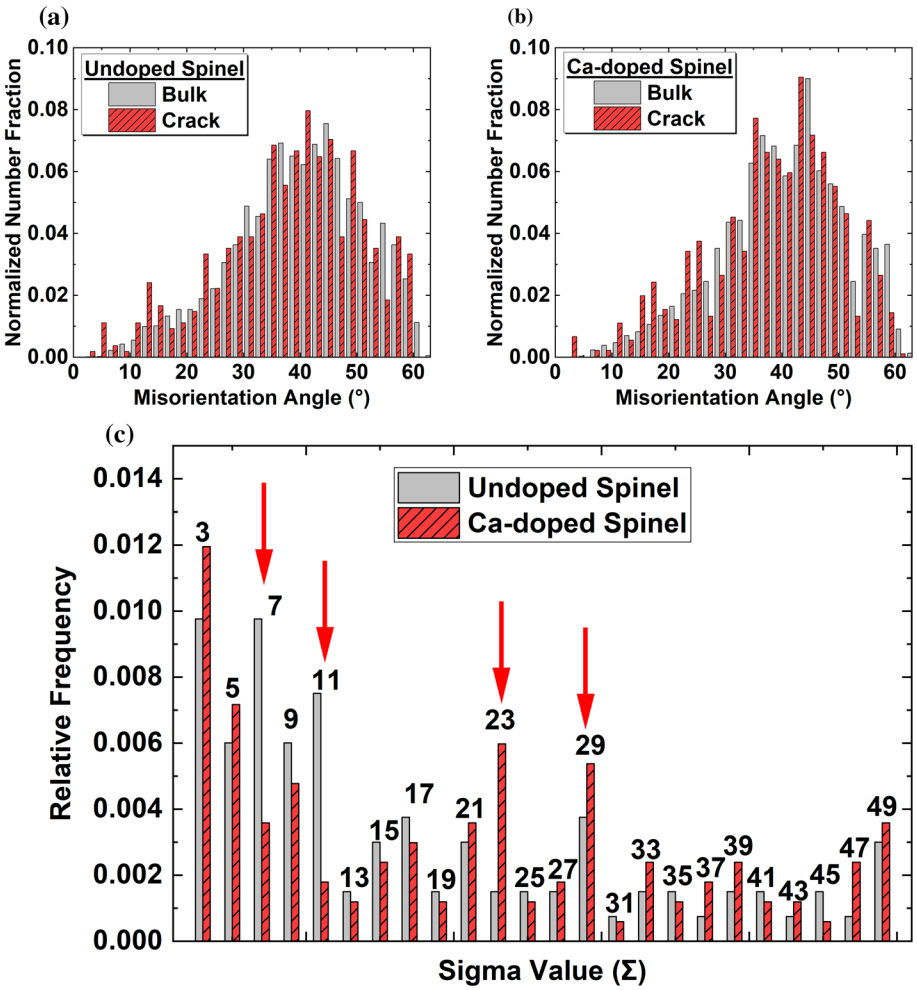

Figure 11 Histograms of the distribution of misorientation angles of grains in the bulk and grain that suffered intergranular fracture in **a** undoped and **b** Ca-doped spinel samples after annealing at 1400 °C for 48 h. **c** Distribution of coincident site lattice (CSL) grain boundaries along the crack path for undoped and Ca-doped spinel samples after annealing at 1400 °C for 48 h. The histograms in **a** and **b** corresponding to the bulk were calculated from grain boundary segments extracted from the EBSD maps using the analysis procedure described by Saylor et al. [22]. The histograms corresponding to grain boundaries along the cracks were normalized by removing the contribution of transgranular fractured grains. The misorientation angle bin size is 2°.

fraction of this large grain size population, any appropriate statistically significant evaluation is not possible from the current results. Therefore, the segregation behavior of this second grain size population and its effect on the mechanical properties requires further investigation.

The quantitative XEDS analysis showed that calcium segregation was found in all 18 grain boundaries for Ca-doped spinel. These results are reasonable considering the larger ionic size of Ca^{2+} cations ($r_i = 100$ pm) as compared to the Mg^{2+} ($r_i = 57$ and 72 pm in the tetrahedral and octahedral sites, respectively) and Al^{3+} ($r_i = 39$ and 54 pm in the tetrahedral and octahedral sites, respectively) [4]. This difference in the ionic radii implied that the calcium segregation was limited to the boundary core, where cations with large ionic size difference can be accommodated by the larger free volume available at the boundary compared to the bulk. The magnesium concentration at the boundary was systematically lower than the bulk (and the off-boundary locations). The aluminum concentration was higher on the boundary compared to the bulk. The magnesium to aluminum concentration ratio (Mg/Al) in normal stoichiometric spinel is 0.5. Based on the quantitative analysis shown in Fig. 3, the Mg/Al ratio varied from 0.485 ± 0.013 in the bulk to 0.478 ± 0.04 in the off-boundary position and finally to 0.448 ± 0.04 at the grain boundary position for Ca-doped spinel (all measurements with a 99% confidence limit (± 3σ)), which confirm the presence on non-stoichiometry at grain boundaries for the Ca-doped spinel sample.

The EELS results provided a more refined view of the concentration profile of the different constituent elements in the vicinity of the grain boundary. The spatial resolution for the EELS analysis was approximately ~ 2 nm (much better lateral resolution than the XEDS analysis where a box size of 12 × 75 nm^2 was

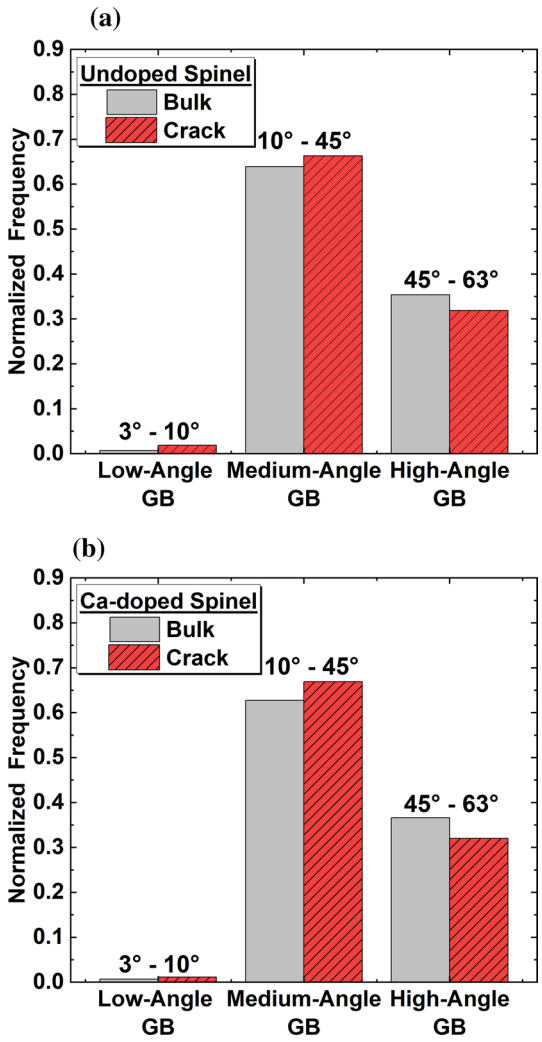

Figure 12 Normalized frequency of grain boundary types with respect to the misorientation angles in the bulk and along the crack path for **a** undoped and **b** Ca-doped spinel samples.

used to acquire the spectra). The EELS results in Fig. 6 showed that more subtle differences in composition were found at grain boundary cores of undoped and Ca-doped spinel compared to the XEDS analysis. Non-stoichiometry in the bulk [34, 35], as well as in the vicinity of grain boundaries [7, 25–28], has been previously studied in spinel using relative quantitative analysis. However, most of these studies focused on undoped specimens. There is a general agreement in the published literature on spinel that the Mg/Al and the Mg/O ratios decrease at the grain boundaries while the O/Al ratio remains constant. The observations in this current research are in good agreement with the literature as can be implied from the concentration profiles in Fig. 6. Additionally, the space-charge layer (and consequently the segregation behavior) of host ions in spinel can be dependent on the MgO/Al_2O_3 ratio of the bulk. Accurately determining this composition ratio is not trivial, especially for samples with slight deviations from stoichiometry. However, the quantification of the EELS data was in good agreement with the XEDS-quantified results. In both cases, the Mg/Al ratio decreased at the grain boundary core compared to the bulk.

The changes in the Mg–K edge ELNES spectra provided additional evidence that more significant changes in the bonding state occurred in the magnesium sublattice at the grain boundaries. In Fig. 7e, a considerable change in the intensity of the A′ prepeak at the grain boundary core in the Ca-doped spinel specimen can be observed, which is not observed in undoped spinel. However, a thorough theoretical-based analysis is necessary to investigate the effect of calcium on the Mg–K edge ELNES further. Additionally, no chemical shift in the O-K edge was found at grain boundaries in Ca-doped spinel based on the maximum energy resolution achieved in the ELNES analysis. In a study by Ikuhara et al. [36], it was demonstrated that SiO_2 doping can produce a chemical shift in the O-K edge at grain boundaries in tetragonal zirconia polycrystal, which can be linked to a bonding strengthening effect that explained the enhanced superplastic behavior of this ceramic material. Therefore, no chemical shift in the O-K edge for Ca-doped spinel sample suggests that the oxygen bonding status is not significantly affected by the Ca doping. It is worth noting that no evidence of grain boundary embrittlement was found according to the fracture behavior analysis.

Based on the observations by quantitative XEDS and EELS analysis, it is implied that Ca^{2+} cations replace Mg^{2+} atoms at tetrahedral sites in Ca-doped spinel, as shown in Fig. 13a. Several arguments can be put forward to justify this inference. First, the EELS analysis shown in Figs. 5d, e indicated that regions of the same boundary with higher calcium concentration presented more significant magnesium depletion. In contrast, the aluminum concentration is slightly higher in Ca-doped spinel compared to undoped spinel (Figs. 4e and 5f). Therefore, calcium and magnesium concentrations are correlated to each other. Second, aluminum excess was found in the vicinity of the boundary (Fig. 5f), which indicates that calcium substituting aluminum is unlikely. This behavior can also be explained by the large difference in ionic

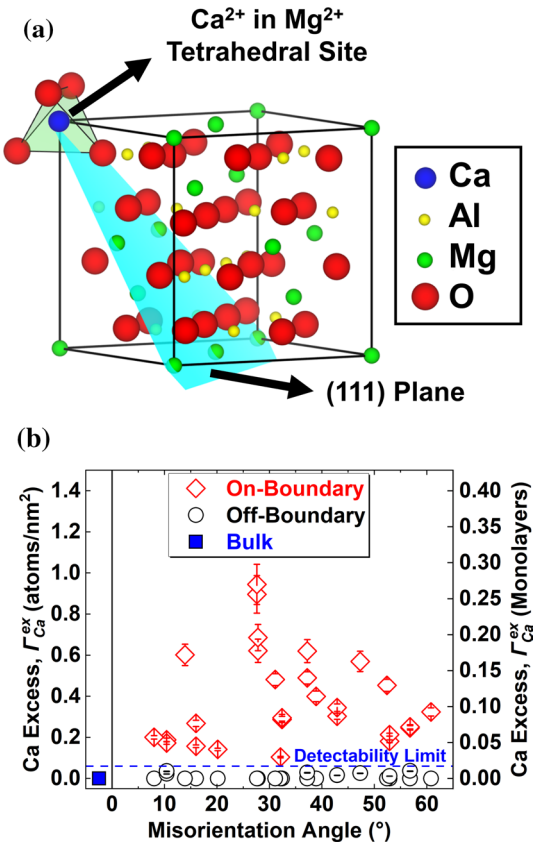

Figure 13 **a** Schematic spinel structure showing the position of Ca^{2+} cations at Mg^{2+} tetrahedral sites. The spinel structure was simulated using VESTA software and the (111) planes is shown in cyan [39]. **b** Calcium excess at grain boundaries in Ca-doped spinel obtained by quantitative XEDS analysis using the ζ-factor method based on the results shown in Fig. 3. The off-boundary condition corresponds to a distance away from the grain boundary of ~ 28 nm and the bulk condition corresponds to grain interior several hundreds of nanometers away from the grain boundary. A (111) boundary plane was assumed to calculate the number of monolayers. The error bars represent a 99% confidence limit (±3σ), and the detectability limit for calcium was 0.03 ± 0.02 at%, equivalent to ~ 0.06 atoms/nm^2.

radius for octahedral site between Ca^{2+} (100 pm) and Al^{3+} (54 pm) which is beyond the 15% allowed limit per Hume-Rothery rules. Third, the concentration profiles for magnesium and calcium in Fig. 6b presented similar shapes, while the aluminum concentration appeared broader, which can be the direct evidence that the magnesium and calcium concentrations are correlated to each other. Fourth, calcium cation (with a 2 + valence state) can occupy Mg^{2+} sites while maintaining the same ionization state 2 + . Therefore, no additional structural defects need to be created by replacing magnesium atoms with calcium, i.e., maintaining the charge neutrality and a minimum energy penalty for the segregation process. Finally, the most significant changes in the bonding state at the grain boundary were found in the Mg–K edge of the ELNES for Ca-doped spinel (Fig. 7e), which suggests that calcium segregation could be linked to such changes.

As presented in Fig. 3a, the measured calcium concentration will vary with specimen thickness, the incident electron probe size, grain boundary inclination, etc. Consequently, the calcium concentration values do not provide a quantitative insight into the grain boundary enrichment. For this reason, the calcium excess at grain boundaries (or the grain boundary enrichment) was calculated. Based on the observations by quantitative XEDS and EELS analysis, it is implied that Ca^{2+} cations replace Mg^{2+} cations at tetrahedral sites in spinel, as discussed above. Therefore, the calcium excess Γ_{Ca}^{ex} can be calculated by specifying Eq. (1) as follows:

$$\Gamma_{Ca}^{ex} = N_{Mg} \frac{X_{Ca}^{gb} - X_{Ca}^{bk}}{X_{Mg}} \frac{V}{A} \tag{8}$$

Here, N_{Mg} is 15.1 Mg atoms per nm^3 in spinel [37], and X_{Ca}^{gb} is the atomic fraction of calcium at the grain boundary obtained by quantitative XEDS analysis through the ζ-factor method (Fig. 3a), X_{Ca}^{bk} is considered as 0 since no calcium was found in the off-boundary positions or the bulk considering the minimum detectability limit of the quantitative analysis (approximate 0.03 ± 0.02 at% for calcium using the Ca-Kα peak), and X_{Mg} is the atomic fraction of magnesium in the off-boundary position). Additionally, a (111) boundary plane with a magnesium occupancy of 3.5 atoms/nm^2 was assumed for calculating the number of monolayers as shown in Fig. 13a. The selection of the boundary planes was based on previous studies in spinel that indicated that {111} is the most prevalent set of grain boundary planes [38].

Quantitative XEDS analysis through the ζ-factor method shown in Fig. 13b indicated that the calcium excess was in the range of ~ 0.1—0.9 atoms/nm^2, corresponding to a maximum coverage of ~ 0.26 monolayers. Additionally, the detectability limit for calcium was about ~ 0.06 Ca atoms/nm^2 dashed blue line in Fig. 13b, which confirms that all grain boundaries analyzed presented calcium segregation above the detectability limit. The grain boundary segregation

behavior might have a strong dependency on other grain boundary characteristics such as boundary plane, tilt/twist character, and ultimately the free volume at the interface available for dopants to segregate, which were not determined in this study.

Effect of Ca-doping on the mechanical properties in spinel

The internal stresses developed due to the synthesis of the samples by hot-pressing were most likely relieved on annealing for 48 h at 1400 °C. These internal stresses can affect the mechanical properties, so that the effect of the calcium segregation could have been masked. Hence, the discussion will be focused on those samples annealed for 48 h to perform a more reliable comparative study.

The indentation fracture toughness was nearly similar for the samples annealed for 48 h at 1400 °C (Fig. 8), which could indicate that Ca^{2+} cations occupying Mg^{2+} sites in the grain boundaries had no significant detrimental effect on the bulk fracture toughness. However, microcantilever bend tests of individual grain boundaries are necessary to directly correlate the calcium segregation behavior with the grain boundary mechanical properties [5, 6]. Alternatively, the accurate K_{Ic} values can be compared with results from mechanical testing with SEPB [40].

Regarding the crack propagation behavior, the normalized number of transgranular fracture events per crack was slightly higher after doping with calcium compared to undoped spinel (Fig. 10b). Both undoped and Ca-doped spinel presented cracks with a mixture of intergranular and transgranular fractures. The quantitative EBSD analysis showed that the fracture behavior was predominantly transgranular, with more than 60% of the total crack length propagating through the grains. Ceramic materials can present different fracture behaviors based on the average grain size. Nanocrystalline ceramics are characterized by a predominant intergranular fracture behavior (cracks propagating through the grain boundaries), as exemplified by Bokov and co-workers in yttria-stabilized zirconia with an average grain size of ~ 20 nm [41]. Conversely, coarse-grain microstructures, in the order of tens or hundreds of micrometers, present mainly transgranular fracture [42]. Spinel materials with medium grain sizes used in this study (undoped: 870 nm and Ca-doped: 700 nm) can be expected to be in a transition zone between these two fracture behaviors. Therefore, it is reasonable to obtain a mixture of intergranular and transgranular fracture modes in this study. Using a quantitative EBSD analysis was crucial to provide additional insights regarding the individual contributions of these two fracture modes, as opposed to qualitative fractography analysis.

A simulation work by Zhou et al. has demonstrated that, for a material with a similar average grain size, the fracture behavior can also be linked to the grain boundary fracture toughness and grain interior fracture toughness [43]. When the ratio of grain boundary to grain interior fracture toughness is between 0.72—0.82, the authors found that cracks propagated with a mixture behavior of intergranular and transgranular fracture. The crack mode became fully transgranular only when the grain boundary fracture toughness increased with respect to the grain interior. This highlights the potential of controlling the fracture behavior by enhancing the grain boundary fracture toughness through grain boundary segregation.

The misorientation angle distributions in the bulk and along the crack for grains with intergranular fracture were similar for both samples, with and without Ca-doping (Fig. 11). Any tendency for a specific grain boundary to present intergranular fracture will appear as a higher number fraction compared to the same grain boundary in the bulk. This study found that the misorientation angle of grains contributing to intergranular crack path follows a similar distribution for undoped and Ca-doped spinel without any preference for specific orientations. In both cases the distributions approached the bulk distribution. Therefore, it was concluded that calcium doping did not lead to preferential grain boundary embrittlement.

Conclusion

The effect of 500 ppm of calcium doping on the segregation behavior and fracture response in spinel was quantitatively analyzed. The main findings through this study can be summarized as follows:

- Quantitative EELS analysis revealed magnesium depletion and aluminum excess at grain boundaries, which suggests that Ca^{2+} cations most likely occupy Mg^{2+} tetrahedral sites at grain boundaries. This observation is supported by similar concentration profile shapes obtained by EELS-SI data-

sets and the same 2 + ionization state for both magnesium and calcium cations.

- Qualitative ELNES analysis revealed differences between the grain boundary core and the vicinity of the grain boundary (~ 1 nm away from the grain boundary) for the Mg–K edge in Ca-doped spinel, which indicated that changes in the bonding status for the magnesium sublattice were observed at the boundary core after calcium doping as compared to the undoped spinel. Further quantitative analysis with theoretical assistance is necessary to conclude whether these changes can be attributed to changes in the grain boundary cohesion.
- Calcium segregation at grain boundaries in spinel was quantified by XEDS analysis, showing no strong dependency on the misorientation angle. Quantitative analysis using the ζ-factor method revealed levels of calcium segregation in all grain boundaries analyzed, ranging from ~ 0.1 to 0.9 atoms/nm^2 (0.03—0.26 monolayers).
- EBSD analysis of the microstructures around the crack paths revealed that calcium doping did not detrimentally affect the number of transgranular cracking events compared to undoped spinel. Additionally, no preferential intergranular cracking at specific misorientation angles was observed in the Ca-doped spinel compared to the undoped condition.
- After 48 h of annealing, the undoped and Ca-doped spinel samples showed similar fracture toughness. This suggests that the incorporation of Ca^{2+} cations in the grain boundaries occupying Mg^{2+} sites did not negatively affect the bulk fracture toughness. However, further mechanical characterizations of individual grain boundaries are necessary to directly correlate the calcium segregation behavior with the grain boundary mechanical properties.
- The findings of this study provided new quantitative insights into how phenomena at the nanoscale, such as the segregation behavior of doping atoms, are closely related to the mechanical response at the microscale, such as microhardness, indentation fracture toughness, and fracture behavior. The unique combination of advanced electron microscopy techniques and detailed quantitative fracture behavior by EBSD can lead to a more predictable way of selecting dopant atoms for enhanced properties in spinel, such as high fracture toughness.

Acknowledgements

This work was supported by the National Science Foundation through grants DMR-2018683, CMMI-2016279 and DMR-2215267. The authors wish to acknowledge the insightful discussions with Dr. Gregory Rohrer regarding quantitative EBSD analysis.

Author contributions

Alexander Campos-Quiros: Conceptualization, Methodology, Software, Validation, Formal Analysis, Investigation, Data Curation, Writing – Original Draft, Visualization. Metri Zughbi: Methodology, Software, Validation, Formal Analysis, Investigation, Data Curation. Animesh Kundu: Conceptualization, Methodology, Validation, Investigation, Resources, Writing – Review and Editing, Supervision, Project Administration, Funding Acquisition. Masashi Watanabe: Conceptualization, Methodology, Software, Validation, Investigation, Resources, Writing – Review and Editing, Supervision, Project Administration, Funding Acquisition.

Funding

National Science Foundation, DMR-2018683, Masashi Watanabe, CMMI-2016279, Masashi Watanabe, DMR-2215267, Masashi Watanabe

Data availability

The data that support the findings of this study are available from the corresponding author upon reasonable request.

Declarations

Conflict of interest The authors declare that they have no known competing financial interests or personal relationships that could have appeared to influence the work reported in this paper.

Supplementary Information The online version contains supplementary material available at https://doi.org/10.1007/s10853-024-10171-z.

References

[1] Salem JA (2013) Transparent armor ceramics as spacecraft windows. J Am Ceram Soc 96:281–289. https://doi.org/10.1111/jace.12089

[2] Rubat du Merac M, Kleebe HJ, Müller MM, Reimanis IE (2013) Fifty years of research and development coming to fruition; Unraveling the complex interactions during processing of transparent magnesium aluminate (MgAl2O4) spinel. J Am Ceram Soc 96:3341–3365. https://doi.org/10.1111/jace.12637

[3] Shi Z, Zhao Q, Guo B, Ji T, Wang H (2020) A review on processing polycrystalline magnesium aluminate spinel (MgAl2O4): Sintering techniques, material properties and machinability. Mater Des 193:108858. https://doi.org/10.1016/j.matdes.2020.108858

[4] Shannon RD (1976) Revised effective ionic radii and systematic studies of interatomic distances in halides and chalcogenides. Acta Cryst A 32:751–767. https://doi.org/10.1107/S0567739476001551

[5] Cao W, Kundu A, Yu Z, Harmer MP, Vinci RP (2013) Direct correlations between fracture toughness and grain boundary segregation behavior in ytterbium-doped magnesium aluminate spinel. Scr Mater 69:81–84. https://doi.org/10.1016/j.scriptamat.2013.03.002

[6] Cui FY, Kundu A, Krause A, Harmer MP, Vinci, (2018) Surface energies, segregation, and fracture behavior of magnesium aluminate spinel low-index grain boundary planes. Acta Mater 148:320–329. https://doi.org/10.1016/j.actamat.2018.01.039

[7] Chiang Y-M, David Kingery W (1990) Grain-Boundary Migration in Nonstoichiometric Solid Solutions of Magnesium Aluminate Spinel: II, Effects of Grain-Boundary Nonstoichiometry. J Am Ceram Soc 73:1153–1158. https://doi.org/10.1111/j.1151-2916.1990.tb05172.x

[8] Kim JM, Kim HN, Park YJ, Ko JW, Lee JW, Kim HD (2016) Microstructure and optical properties of transparent MgAl2O4 prepared by Ca-infiltrated slip-casting and sinter-HIP process. J Eur Ceram Soc 36:2027–2034. https://doi.org/10.1016/j.jeurceramsoc.2016.02.018

[9] Ganesh I, Teja KA, Thiyagarajan N, Johnson R, Reddy BM (2005) Formation and densification behavior of magnesium aluminate spinel: The influence of CaO and moisture in the precursors. J Am Ceram Soc 88:2752–2761. https://doi.org/10.1111/j.1551-2916.2005.00529.x

[10] Kim T, Kim D, Kang S (2014) Effect of additives on the sintering of MgAl2O4. J Alloys Compd 587:594–599. https://doi.org/10.1016/j.jallcom.2013.10.250

[11] Krell A, Hutzler T, Klimke J (2014) Defect strategies for an improved optical quality of transparent ceramics. Opt Mater 38:61–74. https://doi.org/10.1016/j.optmat.2014.09.030

[12] Chan C, Ko Y (1998) Effect of CaO Content on the Hot Strength of Alumina-Spinel Castables in the Temperature Range of 1000° to 1500°C. J Am Ceram Soc 81:2957–2960. https://doi.org/10.1111/j.1151-2916.1998.tb02719.x

[13] Yi S, Huang Z, Huang J, Fang M, Liu Y, Zhang S (2014) Novel calcium hexaluminate/spinel-alumina composites with graded microstructures and mechanical properties. Sci Rep 4:4333. https://doi.org/10.1038/srep04333

[14] West GD, Perkins JM, Lewis MH (2004) Characterisation of fine-grained oxide ceramics. J Mater Sci 39:6687–6704. https://doi.org/10.1023/B:JMSC.0000045600.77776.08

[15] Schumacher O, Marvel CJ, Kelly MN, Cantwell PR, Vinci RP, Rickman JM, Rohrer GS, Harmer MP (2016) Complexion time-temperature-transformation (TTT) diagrams: Opportunities and challenges. Curr Opin Solid State Mater Sci 20:316–323. https://doi.org/10.1016/j.cossms.2016.05.004

[16] Watanabe M, Williams DB (2006) The quantitative analysis of thin specimens: A review of progress from the Cliff-Lorimer to the new ζ-factor methods. J Microsc 221:89–109. https://doi.org/10.1111/j.1365-2818.2006.01549.x

[17] Watanabe M, Egerton RF (2022) Evolution in X-ray analysis from micro to atomic scales in aberration-corrected scanning transmission electron microscopes. Microsc 71:I132–I147. https://doi.org/10.1093/jmicro/dfab026

[18] Watanabe M, Okunishi E, Ishizuka K (2009) Analysis of spectrum-imaging datasets in atomic-resolution electron microscopy. Microsc Anal 23:5–7

[19] Egerton RF (2011) Electron Energy-Loss Spectroscopy in the Electron Microscope, 3rd edn. Springer, New York

[20] ASTM Standard C1327–15 (2019) Standard Test Method for Vickers Indentation Hardness of Advanced Ceramics. ASTM International, West Conshohocken, PA

[21] Miyoshi T, Sagawa N, Sassa T (1985) Study on fracture toughness evaluation for structural ceramics. Trans Jpn Soc Mech Eng A 51:2489–2497. https://doi.org/10.1299/kikaia.51.2489

[22] Saylor DM, El-Dasher BS, Adams BL, Rohrer GS (2004) Measuring the five-parameter grain-boundary distribution from observations of planar sections. Metall Mater Trans 35:1981–1989. https://doi.org/10.1007/s11661-004-0147-z

[23] De Aza AH, Pena P, De Aza S (1999) Ternary system Al2O3-MgO-CaO: I, primary phase field of crystallization of spinel in the subsystem MgAl2O4-CaAl4O7-CaO-MgO. J Am Ceram Soc 82:2193–2203. https://doi.org/10.1111/j.1151-2916.1999.tb02062.x

[24] Romig ADJ, Goldstein JI (1979) Detectability limit and spatial resolution in STEM X-ray analysis: application to

Fe-Ni. In: Newbury DE (ed) Microbeam Analysis – 1979. San Francisco Press, San Francisco, CA, pp 124–128

[25] Benameur N, Bernard-Granger G, Addad A, Raffy S, Guizard C (2011) Sintering analysis of a fine-grained alumina-magnesia spinel powder. J Am Ceram Soc 94:1388–1396. https://doi.org/10.1111/j.1551-2916.2010.04271.x

[26] Halabi M, Ezersky V, Kohn A, Hayun S (2017) Charge distribution in nano-scale grains of magnesium aluminate spinel. J Am Ceram Soc 100:800–811. https://doi.org/10.1111/jace.14610

[27] Nuns N, Béclin F, Crampon J (2009) Grain-Boundary characterization in a nonstoichiometric fine-grained magnesium aluminate spinel: Effects of defect segregation at the space-charge layers. J Am Ceram Soc 92:870–875. https://doi.org/10.1111/j.1551-2916.2008.02901.x

[28] Rufner JF, Kaseman D, Castro RHR, Van Benthem K (2016) DC Electric Field-Enhanced Grain-Boundary Mobility in Magnesium Aluminate during Annealing. J Am Ceram Soc 99:1951–1959. https://doi.org/10.1111/jace.14157

[29] van Benthem K, Kohl H (2000) Methods for ELNES-quantification: characterization of the degree of inversion of Mg–Al-spinels. Micron 31:347–354. https://doi.org/10.1016/S0968-4328(99)00113-4

[30] Quinn GD, Bradt RC (2007) On the vickers indentation fracture toughness Test. J Am Ceram Soc 90:673–680. https://doi.org/10.1111/j.1551-2916.2006.01482.x

[31] Wollmershauser JA, Feigelson BN, Gorzkowski EP, Ellis CT, Goswami R, Qadri SB, Tischler JG, Kub FJ, Everett RK (2014) An extended hardness limit in bulk nanoceramics. Acta Mater 69:9–16. https://doi.org/10.1016/j.actamat.2014.01.030

[32] McColm IJ (1990) Ceramic Hardness. Springer, US, New York

[33] Krause AR, Kundu A, Kosasang O, Vinci RP, Harmer MP (2020) The influence of grain boundary area on the complexion time-temperature-transformation diagram of Eu-doped magnesium aluminate spinel. Scr Mater 178:251–255. https://doi.org/10.1016/j.scriptamat.2019.11.041

[34] Murphy ST, Gilbert CA, Smith R, Mitchell TE, Grimes RW (2010) Non-stoichiometry in MgAl2O4 spinel. Phil Mag 90:1297–1305. https://doi.org/10.1080/14786430903341402

[35] Soeda T, Matsumura S, Kinoshita C, Zaluzec NJ (2000) Cation disordering in magnesium aluminate spinel crystals induced by electron or ion irradiation. J Nucl Mater 283–287:952–956. https://doi.org/10.1016/S0022-3115(00)00164-1

[36] Ikuhara Y, Thavorniti P, Sakuma T (1997) Solute segregation at grain boundaries in superplastic SiO2-doped TZP. Acta Mater 45:5275–5284. https://doi.org/10.1016/S1359-6454(97)00152-3

[37] Sickafus KE, Wills JM, Grimes NW (1999) Structure of spinel. J Am Ceram Soc 82:3279–3292. https://doi.org/10.1111/j.1151-2916.1999.tb02241.x

[38] Miller HM, Saylor D, El Dasher BS, Rollett AD, Rohrer GS (2004) Crystallographic Distribution of Internal Interfaces in Spinel Polycrystals. Mater Sci Forum 467–470:783–788. https://doi.org/10.4028/www.scientific.net/MSF.467-470.783

[39] Momma K, Izumi F (2011) VESTA 3 for three-dimensional visualization of crystal, volumetric and morphology data. J Appl Crystallogr 44:1272–1276. https://doi.org/10.1107/S0021889811038970

[40] Schellenberger A, Belli R, Karsten J, Lohbauer U (2023) On the robustness of the Single-Edge-Precracked-Beam (SEPB) method for fracture toughness testing of ceramic materials. Eng Fract Mech 291:109527. https://doi.org/10.1016/j.engfracmech.2023.109527

[41] Bokov A, Zhang S, Feng L, Dillon SJ, Faller R, Castro RHR (2018) Energetic design of grain boundary networks for toughening of nanocrystalline oxides. J Eur Ceram Soc 38:4260–4267. https://doi.org/10.1016/j.jeurceramsoc.2018.05.007

[42] Borrero-López O, Ortiz AL, Gledhill AD, Guiberteau F, Mroz T, Goldman LM, Padture NP (2012) Microstructural effects on the sliding wear of transparent magnesium-aluminate spinel. J Eur Ceram Soc 32:3143–3149. https://doi.org/10.1016/j.jeurceramsoc.2012.04.002

[43] Zhou J, Chen Y, Feng H, Chen H, Yu X, Liu B (2023) Could effective fracture toughness of polycrystalline aggregates exceed inner grain fracture toughness by adjusting toughness of grain boundary? Eng Fract Mech. https://doi.org/10.1016/j.engfracmech.2023.109170